

Measuring the hadronic spectrum of the quark plasma

Carleton DeTar

Department of Physics, University of Utah, Salt Lake City, Utah 84112

John B. Kogut

Department of Physics, University of Illinois at Urbana-Champaign, 1110 West Green Street, Urbana, Illinois 61801

(Received 6 July 1987)

In an effort to characterize the large-scale structure and composition of the QCD plasma at zero baryon-number density in the vicinity of the high-temperature phase transition, we have carried out a numerical simulation in SU(3) lattice gauge theory with four flavors of low-mass staggered fermions on a 6×10^3 lattice. A small data sample was also collected on $6 \times 10^2 \times 20$ lattices. The simulation uses the Illinois hybrid microcanonical algorithm, adapted for measurements of hadronic screening lengths. Measurements were carried out at three values of the gauge coupling β and at three values each of the bare quark mass. The principal quantities measured are the static screening masses in several color-singlet channels with quark valence $q\bar{q}$ and qqq . Clear evidence for a hadronic screening spectrum is found, suggesting the presence of hadronic plasma modes. The spectral multiplets, extrapolated to zero quark mass, are consistent with a restoration of the $SU(N) \times SU(N)$ chiral symmetry.

I. INTRODUCTION

At high temperature and zero baryon-number density, hadronic matter is expected to undergo a phase change to a new form of matter called the quark plasma. Recent efforts to produce quark matter in high-energy heavy-ion collisions¹ have heightened the importance of developing a solid theoretical understanding of the structure and properties of this novel phase, not merely for its intrinsic theoretical interest, but to suggest and criticize possible experimental signals for plasma formation.

A popular model of the plasma is based upon a naive interpretation of the consequences of asymptotic freedom that obtains an extremely high temperature. According to this "deconfinement folklore," the quark plasma is to be regarded as a gas of weakly interacting quarks and gluons. However, it has been known for some time that long-range nonperturbative effects disrupt this simple picture even at the highest temperatures.^{2,3} Indeed, one of us has proposed that the quark plasma may be "dynamically confined," so that only color-singlet modes produce poles and branch points in linear response functions; i.e., color-singlet modes control the long-distance behavior of plasma disturbances.³ Hadronic plasma modes have also been suggested by Hatsuda and Kunihiro in the context of a Nambu–Jona-Lasinio model, but with quarks also appearing explicitly at low and high temperature.⁴

Studies of the phase boundary separating the low- and high-temperature phases provide additional strong evidence supporting the confined, hadronic nature of the quark plasma.⁵ Recent Monte Carlo simulations suggest the presence of a gap in the phase boundary.^{6–8} (See Fig. 1.) Such a break permits a smooth passage from the low-temperature to the high-temperature regime, and requires that there be a rigorous one-to-one correspondence between the poles and branch points in linear response functions on either side of the phase boundary.

In particular, if quarks and gluons do not give rise to normal threshold branch points in color-singlet response functions at low temperature, they must not be present at high temperature either.

Knowing the long-range structure of the plasma is tantamount to knowing its large-scale composition. A great deal depends upon these degrees of freedom: the equation of state, the rate of entropy production upon a phase change, plasma transport properties, multiplicities and flavors of low-energy particles, and production rates of low-energy lepton pairs, to name a few.

To identify the low-lying modes of excitation of the equilibrium plasma requires studying the finite-temperature, real-time response of the quark plasma:

$$S_{AB}(\mathbf{x}, t) = \langle A(\mathbf{x}, t)B(0, 0) \rangle - \langle A(0, 0) \rangle \langle B(0, 0) \rangle, \quad (1.1)$$

where A and B are local operators and the averages are taken over the Gibbs ensemble at temperature T . Although great strides have been made in developing numerical techniques for simulating the high-temperature statistical ensemble of QCD, we are still unable to simulate real-time response, but must content ourselves with measurements of spacelike, imaginary-time propagation. A useful imaginary-time response function is the correlation product of static operators (static susceptibility)

$$S_{AB}(z) = \langle \bar{A}(z)\bar{B}(0) \rangle - \langle \bar{A}(0) \rangle \langle \bar{B}(0) \rangle, \quad (1.2)$$

where the imaginary-time and transverse-plane averages are given by

$$\bar{A}(z) = \lim_{L \rightarrow \infty} \int_0^\beta d\tau \int_{-L}^L dx \int_{-L}^L dy \frac{A(x, y, z, -i\tau)}{4L^2\beta}.$$

The large-distance behavior of this correlation,

$$S_{AB}(z) \underset{|z| \rightarrow \infty}{\sim} b \exp[-\mu(T)|z|], \quad (1.3)$$

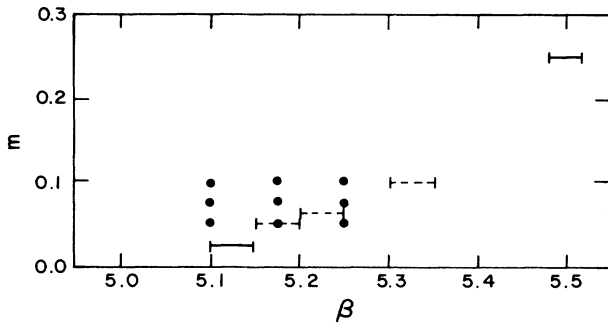


FIG. 1. QCD phase diagram in quark mass vs β . The dots represent the parameter values in the present study. The solid error bars indicate the approximate locations of a first-order phase transition (Refs. 6 and 7). The dotted error bars indicate the location of a rapid crossover in $\langle \bar{q}q \rangle$. The “gap” is in the region of rapid crossover. The phase boundary is thought to extend to high mass from the point at $m \approx 0.25$ and to low mass from the point at $m \approx 0.025$.

gives a screening “mass” or inverse screening length $\mu(T)$.

To see the connection between the screening mass and the real-time response, consider the dispersion relation of one of the normal modes n of the plasma, given by $f_n(k, \omega, T) = 0$, where $k = |\mathbf{k}|$ and ω are the momentum and frequency of the real-time response (1.1). The screening mass obtained in (1.3) is found by analytic continuation to be a solution to

$$f_n[\pm i\mu_n(T), 0, T] = 0$$

for the longest-range mode n in the channel determined by the quantum numbers of the operators A and B .³ Just as the plasmon in an ordinary electrodynamic plasma is associated with the phenomenon of Debye screening, and the pion is associated with the Yukawa potential, so we expect low-lying excitations of the quark plasma to be related to the screening effects that we measure. Of course, such an analytic correspondence tells nothing about the lifetime of the associated real-time excitation. Further arguments are needed to determine the widths.⁶ Hydrodynamic modes present an exceptional case. The phonon and thermal diffusion modes decouple from the energy-density correlation function at zero frequency and so do not appear in the static energy-density correlation or in any of the correlations we measure.⁹ They must, however, be present at nonzero frequency.

To measure the static response function (1.2) of the quark plasma, we have carried out a numerical simulation of QCD on small lattices (6×10^3 and $6 \times 10^2 \times 20$) at temperatures near the phase transition. Measurements were made at three values of the gauge coupling β , namely, 5.10, 5.175, and 5.25, and for each of these, at three values of the bare quark mass m , 0.05, 0.075, and 0.10. Fermions were incorporated in the staggered scheme¹⁰ using a modification of the Illinois hybrid microcanonical algorithm.¹¹ We measured several hadron propagators at large spacelike separation. Although our

methods for measuring hadron correlation functions are well known in studies of the zero-temperature hadron mass spectrum^{12–14} to our knowledge, ours is the first deliberate application of these methods to the quark plasma.

Let us see where our measurements are made in relationship to the phase transition. Shown in the m vs β phase diagram to Fig. 1 are the points at which the simulations were run and the current best estimate for the location of the phase transition for the SU(3)-color, four-flavor, $N_f = 6$ lattice.^{6,7} Since we will be extrapolating results to zero quark mass along lines of constant β , it is important to know which phase is realized in the extrapolation. It is suspected that there is a first-order phase transition at low bare-quark masses $m < 0.025$, as shown, but that the phase transition is not found for $0.10 > m > 0.05$ and $5.35 > \beta > 5.175$. This low-mass phase transition is expected to persist to zero mass, where it is associated with a restoration of the chiral symmetry. At higher quark mass $m > 0.25$ there is again a first-order phase transition, which is expected to persist to infinite quark mass, where it corresponds to the static deconfinement phase transition of the pure gluon theory. The existence of such a gap in the infinite-volume limit in the phase diagram of the four-flavor theory is not firmly established, since its extent in present lattice simulations may be exaggerated by finite-size effects. Nevertheless, for the lattice sizes in the present study, the extrapolation to the zero mass limit should be smooth. Therefore, an extrapolation to $m = 0$ at $\beta = 5.10$ is likely to reach the low-temperature, “deconfined,” broken-chiral-symmetry phase and an extrapolation at the two higher values of β , the high-temperature, “quark plasma,” or chirally symmetric phase, without encountering the singularity associated with the phase transition.

In addition to studying the quantitative variation of the screening masses with temperature and quark mass, a principal objective of this study was to see how the expected high-temperature restoration of chiral symmetry in the quark plasma affects the spectrum of screening masses in the chiral limit of zero quark mass. With N flavors of massless quarks, QCD is symmetric under a chiral $SU(N) \times SU(N) \times U(1) \times U(1)$ group. The $U(1) \times U(1)$ chiral symmetry is explicitly broken by the gauge anomaly, and the $SU(N) \times SU(N)$ symmetry is spontaneously broken at zero temperature, resulting in the appearance of a massless Goldstone boson. A modified version of the Goldstone theorem applies at finite temperature as well, with the Goldstone boson appearing as a zero-frequency excitation at zero wave number, i.e., the screening mass of the Goldstone boson must vanish. A restoration of the $SU(N) \times SU(N)$ symmetry would allow the plasma mode vestige of the corresponding Goldstone boson, should it survive, to have a nonzero gap frequency, and therefore nonvanishing screening mass.

It has been argued that both chiral symmetries are restored at high temperature.¹⁵ Although the restoration of $SU(N) \times SU(N)$ is likely to occur through a phase transition, the gauge anomaly occurs at all temperatures, so that the restoration of $U(1) \times U(1)$ is apt to be only

TABLE I. Expected $SU(2) \times SU(2)$ chiral multiplets.

π - σ
b_1 - ω
ρ - a_1
$N(\frac{1}{2}^+) - N(\frac{1}{2}^-)$

asymptotic. Nevertheless, a suppression of the gauge anomaly through a phase transition could lead to interesting consequences.¹⁶

It has been known for some time from numerical simulations that the flavor-singlet chiral-order parameter $\langle \bar{q}q \rangle$ drops abruptly with increasing temperature at the supposed phase transition in QCD (Ref. 6). Such behavior signals a restoration of either the $SU(N) \times SU(N)$ symmetry or the $U(1) \times U(1)$ symmetry or both. Furthermore, symmetry restoration requires the formation of chiral multiplets of states related by the larger symmetry. One way to discover which symmetry is restored is to examine the multiplet structure of the excitations in the high-temperature phase (Table I). It is obvious that when a symmetry is manifest, i.e., the density matrix is invariant under the symmetry transformation, hadron channels related by symmetry must have identical spectral properties and, in particular, identical screening masses. The chiral-multiplet structure is determined explicitly by the valence-quark assignments for the various states. We describe the calculation, the measurement of the static correlations, and the fitting process in Sec. II. In Sec. III we discuss the extrapolation to the chiral limit and present the main numerical results. Section IV gives our conclusions. A synopsis of our results has been given in a Letter.¹⁷ Here methods are described and detailed results given.

II. DATA COLLECTION AND FITTING

A. Algorithm, parameters, and data sample

Simulations were carried out with the Illinois hybrid microcanonical algorithm,⁶ using the following parameter choices. The microcanonical time step was $dt = 0.02$, the interval for random refreshing of the gauge field was $\Delta t = 0.74$, and the interval for the pseudofermion field was $\Delta t = 0.60$. Evolution of the pseudofermion field was computed using the conjugate-gradient algorithm with a residual tolerance of 5×10^{-4} for the microcanonical evolution.¹⁸ Hadron propagators and various other observables were computed at intervals of $\Delta t = 1$ and saved for subsequent analysis. For this purpose a second conjugate-gradient inversion was necessary to compute the quark propagator. To assure sufficient convergence in this step, the residual tolerance in the conjugate-gradient inversion was set to 2×10^{-4} in most instances on the 6×10^3 lattice and to 2×10^{-5} on the $6 \times 10^2 \times 20$ lattice.

The size and scope of the data sample are summarized in Table II. To increase the distance of hadron propaga-

TABLE II. Scope of the data sample.

Lattice	β	m	Iterations (thousands)	Microcanonical time
6×10^3	5.10	0.05	14.5	290
		0.075	13.5	270
		0.10	9	180
	5.175	0.05	35	700
		0.075	25	500
		0.10	10	200
	5.25	0.05	32.5	575
		0.075	15	300
		0.10	16.5	330
$6 \times 10^2 \times 20$	5.10	0.05	2.5	50
		0.075	2	40
		0.10	1	20
	5.175	0.05	3	60
		0.075	2	40
		0.10	1.5	30
	5.25	0.05	3	60
		0.075	2.5	50
		0.10	3	60

tion, all lattices were doubled in the z direction by replicating the gauge-field configuration. This step is taken at the risk of introducing some systematic finite-size errors, which we discuss below. Because periodic boundary conditions were used, the greatest effective distance of propagation on the doubled 6×10^3 lattices was 10 lattice units and on the doubled $6 \times 10^2 \times 20$, 20 lattice units.

B. State propagators for mesons and baryons

In this study we consider only hadron operators formed from local products of quark operators. The basic meson operator is thus

$$M(\mathbf{r}, \tau) = \bar{\chi}_\alpha(\mathbf{r}, \tau) \chi_\alpha(\mathbf{r}, \tau),$$

where $\chi_\alpha(\mathbf{r}, \tau)$ is the one-component fermion Grassman field with color index α . The basic meson correlation product is

$$S(\mathbf{r}, \tau) = \langle M(\mathbf{0}, 0) M(\mathbf{r}, \tau) \rangle_v. \quad (2.1)$$

The subscript v in (2.1) indicates that only the quark valence part of the propagator is computed; i.e., the correlation product is pieced together from the quark propagator from $(\mathbf{0}, 0)$ to (\mathbf{r}, τ) and the antiquark propagator between the same end points. The restriction to the quark valence part of the propagator affects only the propagation of the mesons with vacuum quantum numbers, i.e., only the σ meson in our study. In that case, omitting the quark-antiquark annihilation part, i.e., the mixing with the glueball of the same quantum numbers, distorts the propagator. For this reason we have labeled the σ screening masses σ_v . To obtain the omitted glueball component requires considerably more computational effort, and is left for future work. At zero-quark mass in the high-temperature phase in which the chiral sym-

metry is restored, glueball mixing is forbidden by chiral selection rules. Therefore, this deficiency does not alter the end point of our extrapolation to the chiral limit in the high-temperature phase and does not affect the identification of chiral multiplets in the propagators we measure. However, at least to some degree, it does affect the determination of screening masses for the σ meson in the low-temperature phase and at nonzero bare-quark mass.

The projection onto channels with various quantum numbers is readily adapted from the zero-temperature analysis. We define the six correlation functions:

$$S_{ps}(z) = \sum_{x,y,\tau} S(x,y,z,\tau), \quad (2.2)$$

$$S_{vt0}(z) = \sum_{x,y,\tau} (-)^{\tau} S(x,y,z,\tau), \quad (2.3)$$

$$S_{vt1}(z) = \sum_{x,y,\tau} [(-)^x + (-)^y] S(x,y,z,\tau), \quad (2.4)$$

$$S_{pv0}(z) = \sum_{x,y,\tau} (-)^{x+y} S(x,y,z,\tau), \quad (2.5)$$

$$S_{pv1}(z) = \sum_{x,y,\tau} [(-)^y + (-)^{x+\tau}] S(x,y,z,\tau), \quad (2.6)$$

$$S_s(z) = \sum_{x,y,\tau} (-)^{x+y+z+\tau} S(x,y,z,\tau). \quad (2.7)$$

The subscripts 0 and 1 refer to the helicity components for the vector and pseudovector mesons. The helicity is the component of angular momentum about the z direction, the direction of the momentum vector. Using the methods of Ref. 19, it is straightforward to determine the above phases appropriate to the relevant Dirac matrices.

The above correlation functions are then fit to a series of nonoscillating and oscillating spectral terms of the general form

$$T_n(z) = b_n \{ \exp(-\mu_n z) + \exp[-\mu_n(L-z)] \},$$

$$U_n(z) = b_n (-)^z \{ \exp(-\mu_n z) + \exp[-\mu_n(L-z)] \},$$

where $L=20$ for the smaller lattice and 40 for the larger lattice. The fitting functions are

$$S_{\text{fit},ps}(z) = T_{\pi}(z) + T_{\pi'}(z), \quad (2.8)$$

$$S_{\text{fit},vt0}(z) = T_{\rho_0}(z) + U_{b_{10}}(z), \quad (2.9)$$

$$S_{\text{fit},vt1}(z) = T_{\rho_1}(z) + U_{b_{11}}(z), \quad (2.10)$$

$$S_{\text{fit},pv0}(z) = T_{a_{10}}(z) + U_{\rho'_0}(z), \quad (2.11)$$

$$S_{\text{fit},pv1}(z) = T_{a_{11}}(z) + U_{\rho'_1}(z), \quad (2.12)$$

$$S_{\text{fit},s}(z) = T_{\sigma_v}(z) + U_{\pi''}(z). \quad (2.13)$$

The measured data $S(z)$ is folded to the interval $z \in [0, L/2]$ before fitting. We have used the familiar language of SU(2) flavor to label the screening masses. The above expressions are similar to those used in determining the hadron mass spectrum,^{12,19} except that the z direction is the direction of propagation, and there is a

splitting of the helicity 0 and 1 channels for the vector and pseudovector mesons, owing to the breakdown of full Lorentz invariance in the medium.

In principle, the ρ meson couples to both the vt and pv channels and the π meson couples to both the ps and s channels. One technique for reducing the number of fitted parameters¹² is to force $\mu_{\pi} = \mu_{\pi''}$, $\mu_{\rho_0} = \mu_{\rho'_0}$, and $\mu_{\rho_1} = \mu_{\rho'_1}$. We preferred instead to allow the ‘‘duplicate’’ masses to vary freely in the fitting process. We routinely threw out the measured points for small values of z in order to reduce the influence of higher spectral components. If we allowed all masses to vary freely, we found consistent results when we started the fit at an even or an odd value of z . Forcing the masses to agree introduced unwanted biases in the determination of the nonoscillating spectral components. Furthermore, forcing equality presumes that the specified component is indeed strongly present in both channels, which may not be the case. This point is discussed further in the next section.

The expressions for the baryon correlation are also similar to those used in determining the hadron mass spectrum, except that propagation is in the periodic z direction, and it is necessary to compensate for antiperiodicity in the average over the imaginary-time direction.¹⁴ The basic baryon operator is

$$B(\mathbf{r}, \tau) = \epsilon_{\alpha\beta\gamma} \chi_{\alpha}(\mathbf{r}, \tau) \chi_{\beta}(\mathbf{r}, \tau) \chi_{\gamma}(\mathbf{r}, \tau)$$

and the baryon static correlation

$$S_B(\mathbf{r}, \tau) = \langle B(\mathbf{0}, 0) B(\mathbf{r}, \tau) \rangle$$

is averaged over imaginary time at the lowest fermion Matsubara frequency πT and over the spatial directions x and y as

$$S_B(z) = \sum_{x,y,\tau} \cos(\pi\tau/N_{\tau}) B(x,y,z,\tau),$$

where $N_{\tau}=6$ for our lattices. This correlation function is then fit to the form

$$\begin{aligned} S_{\text{fit},B}(z) = & b_{N_+} \{ (-)^z \exp(-\mu_{\text{eff},N_+} z) \\ & + \exp[-\mu_{\text{eff},N_+}(L-z)] \} \\ & + b_{N_-} \{ \exp(-\mu_{\text{eff},N_-} z) \\ & + (-)^z \exp[-\mu_{\text{eff},N_-}(L-z)] \}, \quad (2.14) \end{aligned}$$

where the effective screening masses thus obtained must be corrected for fermion antiperiodic boundary conditions to get the ‘‘physical’’ screening masses μ_{N_+} and μ_{N_-} as

$$(\mu_{\text{eff},N})^2 = \mu_{N^2} + \sin^2(\pi/N_{\tau}).$$

For the effective masses determined in this study, the correction is insignificant.

C. Correlations, covariances, and statistical errors

To assure proper equilibration of the lattices, wherever possible, starting lattices were taken from previous

long runs, or from runs at adjacent parameter values. For the $6 \times 10^2 \times 20$ lattices starting configurations were obtained by doubling a previously equilibrated 6×10^3 lattice. In most cases a few thousand microcanonical iterations representing a time sequence of 50 to 100 units were discarded before taking measurements. The parameter $\langle \bar{q}q \rangle$ measured from the pseudofermion field is quite slow to equilibrate and was used as an indicator of equilibrium. Furthermore, for the 6×10^3 lattices quite long runs were made to guard against overlooking long-time correlations. Because the runs for the $6 \times 10^2 \times 20$ lattices were short, this assurance was not always possible. For this reason measurements on the larger lattices were used only to cross-check some of the results found on the smaller lattices.

A careful analysis is required to determine the systematic and statistical errors in the screening masses.²⁰ There are strong correlations in the measurements of all observables over microcanonical time t and over distance z . Because measurements of observables were taken at regular intervals of one time unit, in all cases considerably less than the decay time of the time correlation, the time series could be followed and the decay of the fluctuations could be studied. Among all of the propagators, the propagator $S_s(z)$ was found to have the longest decay time, taking typically about 10 time units or less to decay. However, at $\beta=5.175$ and $m=0.05$, the decay time was 50 time units. This point lies on the cross-over region. (See Fig. 1.) Therefore, this finding can be attributed to an incipient critical slowing down associated with a nearby critical point. Before carrying out further analysis, all of the propagator measurements were accordingly averaged in bins over an interval of 10 or 50 time units (representing 500 or 2500 iterations), as needed, to give observations that we took to be statistically independent in t .

To treat the correlations in z we carried out an analysis of covariance. For each channel in which M independent measurements at microcanonical time bin j were made, define the mean, variance, and normalized residual at each value of z , respectively, as

$$\begin{aligned} \langle S(z) \rangle &= \sum_{j=1}^M S_j(z)/M, \\ \sigma_z^2 &= \sum_{j=1}^M [\langle S_j^2(z) \rangle - \langle S(z) \rangle^2]/(M-1), \\ \Delta_j(z) &= [S_j(z) - \langle S(z) \rangle]/\sigma(z). \end{aligned}$$

The covariance matrix is

$$r(z, z') = \sum_{j=1}^M \Delta_j(z)\Delta_j(z')/(M-1). \tag{2.15}$$

Table III gives a typical covariance matrix for measurements folded on the interval $z \in [0, L/2]$. It is clear that the correlations are extremely strong for measurements at adjacent values of z and fall off rather slowly with separation. A study of the eigenvectors of this matrix (principal factor coefficients) reveals that the fluctuations of the propagator measurements are rather like the modes of a vibrating string with the largest variance associated with a mode in which the points all fluctuate in phase with about equal percentage variation, and the smallest variance associated with a mode with several nodes. The contrast between the largest and smallest principal factor variance is very large. In the case illustrated, the largest three variances are 9.5, 1.2, and 0.12.

Because of these strong correlations in z , it is incorrect to assume that the points measured at different values of z are statistically independent. Therefore, we have used the following definition of χ^2 for fitting the data:

$$\chi^2 = \sum_{z, z'=0}^{L/2} [S(z) - S_{\text{fit}}(z)][S(z') - S_{\text{fit}}(z')]h(z, z')/\sigma(z)\sigma(z'), \tag{2.16}$$

TABLE III. Covariance matrix for measurements of the pion propagator on the 6×10^3 lattice over the distance $z=0$ to $z=10$.

$z=0$	1	2	3	4	5	6	7	8	9	10	z'
1.00	0.93	0.89	0.86	0.80	0.73	0.68	0.63	0.58	0.56	0.57	0
	1.00	0.95	0.90	0.83	0.76	0.70	0.65	0.59	0.57	0.58	1
		1.00	0.97	0.93	0.87	0.82	0.78	0.75	0.73	0.73	2
			1.00	0.98	0.93	0.89	0.86	0.82	0.80	0.80	3
				1.00	0.98	0.95	0.93	0.91	0.89	0.89	4
					1.00	0.99	0.98	0.96	0.95	0.95	5
						1.00	0.99	0.98	0.97	0.97	6
							1.00	0.99	0.99	0.98	7
								1.00	1.00	0.99	8
									1.00	1.00	9
										1.00	10

where $h(z, z') = r^{-1}(z, z')$ is the reciprocal of the covariance matrix. The estimated variance of the best-fit parameter values was obtained in the usual way from the Hessian matrix at the minimum of this statistic. One might expect that using this expression, rather than the usual uncorrelated form, would change the best-fit parameter values and the values of their estimated variances. However, in most cases that we checked the difference was only slight, but the actual value of χ^2 obtained from Eq. (2.16) is certainly more meaningful. As a check of the estimate of statistical errors in the parameter values, the data sample was broken into a few large segments, typically of 50 to 100 or more time units long, the propagator in each segment was fit using (2.16) and the standard deviation from the mean of these values was compared with the values obtained from the Hessian matrix based on the entire data sample. No significant difference was found.

In order to construct a nonsingular covariance matrix (2.15), it is necessary to have at least as many statistically independent observations in j as the dimension of the matrix. Some of the data samples taken with the $6 \times 10^2 \times 20$ lattice were too small to satisfy this requirement. In this case we constructed a nonsingular matrix by the following standard device:²¹ In the spectral decomposition of the covariance matrix, make a trial matrix by keeping only the terms corresponding to the largest one or two eigenvalues (dominant principal factors). Then in this trial matrix replace all of the diagonal elements by one to get the matrix $r(z, z')$. In effect this procedure is intermediate between taking all points uncorrelated and including correlations completely.

D. Other systematic errors

Other systematic errors arise from various sources. Among these are the neglect of higher spectral components and finite-size effects. Shown in Fig. 2 is the correlation function $S_{ps}(z)$ at $\beta = 5.5$ and $m = 0.05$ from the data for the 6×10^3 and $6 \times 10^2 \times 20$ lattices. The fit is to Eq. (2.8) with a single spectral component T_π , starting at $z_{\min} = 4$. To reduce the influence of higher spectral components, several trial fits were made, over the range $z_{\min} \leq z \leq 20$, for $z_{\min} = 0, 1, 2, \dots$. As the starting point for the fit was increased, the fitted value of μ_π

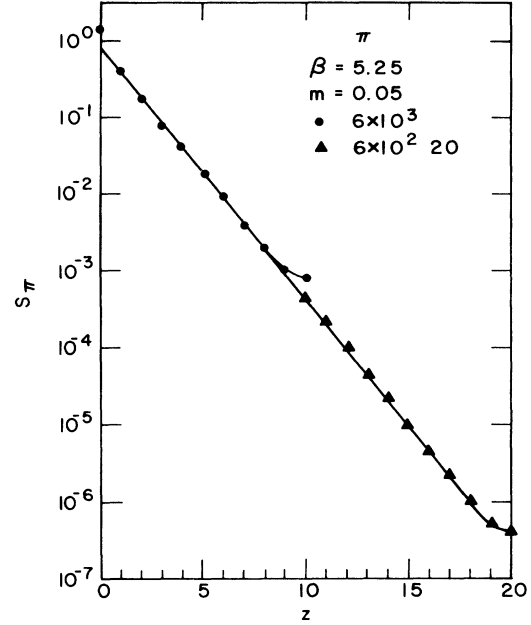


FIG. 2. The static correlation (1.2) in the pion channel, averaged over x and y , as a function of the separation z in the high-temperature phase. The points are from the numerical simulation at $\beta = 5.25$ and quark mass $m = 0.05$ in lattice units. The errors are smaller than the symbol sizes.

decreased. The value of χ^2 also decreased. The process was stopped when the decrease was not larger than $1\frac{1}{2}\sigma$ of the new value.²⁰ As a check of this process, another fit was made with two spectral components, starting at $z = 0$. The value of μ_π for the lower component was found to agree with the value obtained from the single spectral component. This procedure gives us confidence that we have control of systematic errors arising from the neglect of higher spectral components.

The fit to the single spectral component for $z_{\min} = 4$ is good. The larger lattice gives a screening mass of $0.765(3)$ (statistical error only) in lattice units with a $\chi^2/\text{DF} = 29/15$. The smaller lattice gives a screening mass of $0.754(3)$ with $\chi^2/\text{DF} = 20/5$. Because of the small data sample taken for the larger lattice, the

TABLE IV. Summary of measured screening masses on the 6×10^3 lattice: pseudoscalar and scalar mesons and baryons. Also given is the pion screening mass for the $6 \times 10^2 \times 20$ lattice.

β	m	π	π^a	π'	π''	σ_v	$N(\frac{1}{2}^+)$	$N(\frac{1}{2}^-)$
5.10	0.05	0.576(2)	0.5818(3)	1.9(1)	1.3(1)	1.39(3)	2.28(2)	2.63(3)
	0.075	0.694(1)	0.6899(4)		1.4(1)	1.50(6)	2.32(1)	2.67(3)
	0.10	0.784(1)	0.7831(1)		1.5(1)	1.73(2)	2.39(1)	2.85(4)
5.175	0.05	0.625(3)	0.636(1)	1.74(3)	1.06(2)	1.04(2)	2.12(3)	2.23(2)
	0.075	0.713(1)	0.715(1)		1.28(4)	1.30(3)	2.24(2)	2.46(4)
	0.10	0.803(1)	0.802(1)		1.46(3)	1.58(2)	2.35(2)	2.65(6)
5.25	0.05	0.754(3)	0.765(3)	1.65(3)	0.95(4)	0.874(2)	1.91(2)	1.98(2)
	0.075	0.779(3)	0.788(2)	1.70(4)	1.01(5)	1.07(1)	1.99(2)	2.08(4)
	0.10	0.826(4)	0.841(3)		1.28(3)	1.39(2)	2.22(2)	2.44(4)

^aPion screening mass for the $6 \times 10^2 \times 20$ lattice.

TABLE V. Summary of measured screening masses for the 6×10^3 lattice: vector, axial vector, and tensor mesons. See Eqs. (2.8)–(2.13) for a definition of the spectral terms.

β	m	ρ_0	ρ'_0	ρ_1	ρ'_1	a_{10}	a_{11}	b_{10}	b_{11}
5.10	0.05	1.35(4)	1.5(1)	1.30(3)	1.4(1)	1.78(3)	1.78(3)	1.6(1)	1.8(1)
	0.075	1.41(2)	1.57(4)	1.46(2)	1.66(6)	1.90(4)	1.96(3)	1.8(1)	1.9(1)
	0.10	1.42(3)	1.7(1)	1.47(2)	1.63(3)	2.03(3)	1.97(3)	1.9(1)	
5.175	0.05	1.29(1)	1.34(3)	1.23(7)	1.28(2)	1.55(3)	1.46(2)	1.6(1)	1.4(1)
	0.075	1.37(2)	1.52(3)	1.39(2)	1.40(3)	1.82(4)	1.70(7)	1.74(4)	1.40(3)
	0.10	1.40(3)	1.62(2)	1.49(1)	1.55(5)	1.92(7)	1.68(6)	1.3(2)	1.8(1)
5.25	0.05	1.29(2)	1.15(5)	1.20(2)	1.29(4)	1.39(6)	1.29(2)	1.38(5)	1.6(1)
	0.075	1.34(1)	1.37(5)	1.22(2)	1.31(4)	1.58(7)	1.37(6)	1.53(7)	1.6(1)
	0.10	1.36(2)	1.47(3)	1.32(1)	1.48(3)	1.72(6)	1.59(9)	1.4(3)	1.4(4)

discrepancy could be due to either systematic errors arising from disequilibrium or a neglect of long-time correlations in the larger lattice, finite-size effects in the smaller lattice, or a combination of these. A glance at Table IV comparing μ_π for the two lattice sizes reveals similar small discrepancies at all of the gauge couplings and bare quark masses. Thus the systematic errors of this nature could be as large as three times the statistical error. Even so, the combined error in the screening mass appears to be only about one percent in this channel. Because of the small data sample for the larger lattice, screening masses in the other channels were not determined reliably in the larger lattice, and we do not quote those results here.

III. ANALYSIS AND DISCUSSION OF RESULTS

A. Duplicate masses

Tables IV and V summarize the screening masses obtained from the correlation functions by the methods discussed in the previous section. All masses are quoted in lattice units unless otherwise stated. A blank entry in the table indicates that there was not sufficient data to obtain a statistically meaningful value. A few comments are in order.

(1) We found no statistically significant oscillating term in the S_{ps} correlation. In most cases it was possible to extract two spectral components μ_π and $\mu_{\pi'}$ in this channel, both with pion quantum numbers. The determination of the higher-mass component is, of course, very sensitive to systematic errors arising from the neglect of other, still higher-mass components.

(2) The ρ meson appears in both the vt and pv channels. Statistically, the ρ -meson screening mass is better determined in the S_{vt} correlation than in the S_{pv} correlation. Nevertheless, we see that the two determinations

of the ρ screening mass agree within typically three times the stated statistical error. We attribute this discrepancy to systematic errors in extracting the mass from the oscillating term in the S_{pv} propagator. In subsequent analysis we use only the value obtained from the S_{vt} correlation.

(3) The pion component appears in both the ps and s channels. The discrepancy between the screening masses μ_π and $\mu_{\pi'}$ found in the two correlation functions, respectively, is so great in this case that we suspect that they correspond to different states, and that the pion couples only weakly to the S_s correlation function.

B. Extrapolation to the chiral limit

Consider, now, an extrapolation to the chiral limit (bare quark mass $m = 0$). In most cases a linear extrapolation sufficed, and the results are given in Table VI and Figs. 3–8. For the two blank entries a quadratic extrapolation was required, as explained below.

$\beta = 5.10$. At $\beta = 5.10$ (low-temperature phase) chiral perturbation theory requires that the square of the pion screening mass be analytic in the quark mass. A linear fit to $\mu_\pi^2(m)$ yielded $\mu_\pi(0) = 0.055(4)$ with $\chi^2/\text{DF} = 24/1$, a bad fit. A glance at the plotted data in the lower panel of Fig. 3 shows that there is some curvature in $\mu_\pi^2(m)$. Constraining the intercept to be zero, as would be the case for a Goldstone boson, we were able to fit the measured points to the quadratic

$$\mu_\pi^2(m) = 7.21(6)m - 10.5(7)m^2 \quad (3.1)$$

with $\chi^2/\text{DF} = 2.0/1$, an excellent fit, as shown in Fig. 3. Therefore, the data are consistent with the hypothesis that the pionic plasma mode remains a Goldstone boson up to the phase transition. Moreover, the σ meson is

TABLE VI. Linear extrapolation of screening masses to the chiral limit.

β	π	σ_v	ρ_0	ρ_1	a_{10}	a_{11}	$N(\frac{1}{2}^+)$	$N(\frac{1}{2}^-)$
5.10		1.04(6)	1.31(8)	1.20(6)	1.53(7)	1.62(7)	2.16(4)	2.40(7)
5.175	0.445(4)	0.50(4)	1.17(3)	1.06(7)	1.14(9)	1.21(7)	1.89(4)	1.80(7)
5.25	0.674(6)		1.23(4)	1.05(4)	1.07(13)	1.04(9)	1.58(4)	1.54(6)

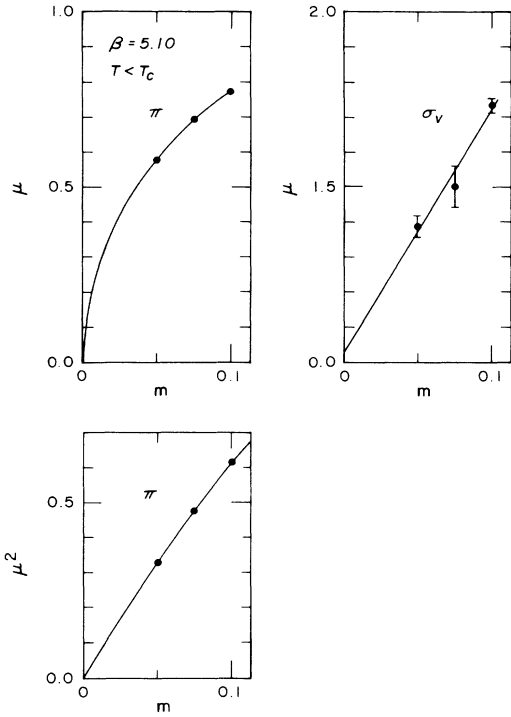


FIG. 3. Pion and σ screening masses at $\beta=5.10$ as a function of bare-quark mass m in lattice units. The pion screening mass is fit to the curve (3.1) and the σ screening mass, to a straight line.

clearly not degenerate with the pion in the chiral limit.

The extrapolated and unextrapolated values for the two helicity states of the ρ meson agree within statistical errors, as do those for the a_1 meson. Therefore, the masses were averaged in each instance and extrapolated, yielding the results

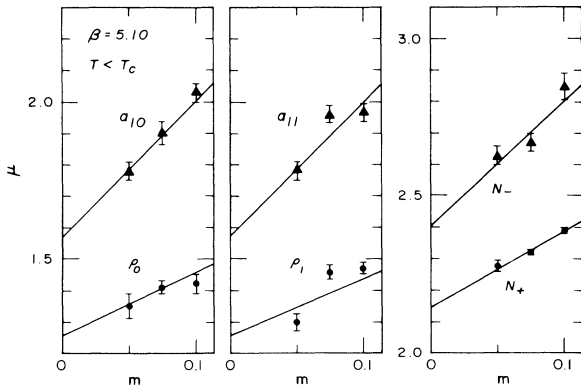


FIG. 4. ρ - and a_1 -meson and nucleon screening masses at $\beta=5.10$ as a function of bare-quark mass m in lattice units. Two helicity states of the mesons and two parity states of the nucleon occur. The meson screening masses are fit to Eq. (3.2), which equates the screening masses for the two helicity components. The nucleon screening masses are fit to a straight line.

$$\begin{aligned}\mu_\rho(m) &= 1.23(10) + 2.4(13)m, \\ \mu_{a_1}(m) &= 1.56(9) + 4.5(13)m\end{aligned}\quad (3.2)$$

with $\chi^2/DF=1.0/1$ and $0.4/1$, respectively. Figure 4 shows these fits. The intercepts are different. The two nucleon screening masses are also statistically different.

In Table VII are summarized measurements of a variety of operator expectation values. A linear extrapolation of $\langle \bar{q}q \rangle$, shown in Fig. 9 gives $0.69(4)$, quite consistent with a nonzero value. In sum we find the extrapolated spectrum and $\langle \bar{q}q \rangle$ to be fully consistent with a spontaneous breakdown of the $SU(N) \times SU(N)$ chiral symmetry at a temperature just below the phase transition.

$\beta=5.175$. If the point $\beta=5.175$ and $m=0$ is in the chirally restored phase, then chiral perturbation theory permits a linear extrapolation of the pion screening mass. Indeed a linear fit yields

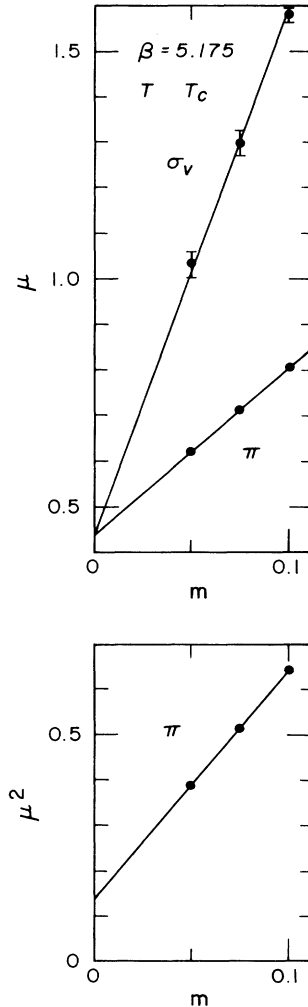


FIG. 5. Pion and σ screening masses at $\beta=5.175$ as a function of bare-quark mass m in lattice units. The pion screening mass is fit to the straight line (3.3) and the σ screening mass, to a straight line with the same intercept as the pion.

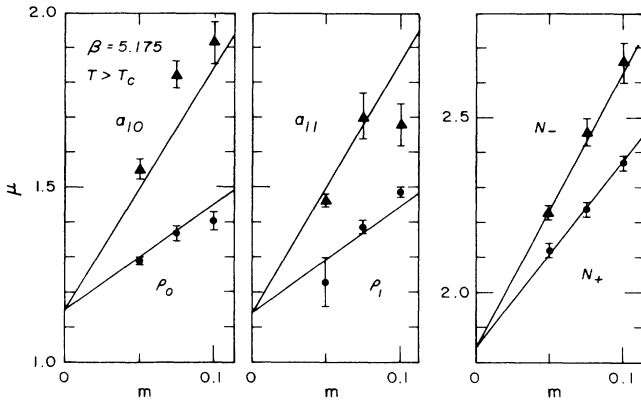


FIG. 6. ρ - and a_1 -meson and nucleon screening masses at $\beta=5.175$ as a function of bare quark mass m in lattice units. Two helicity states of the mesons and two parity states of the nucleon occur. The meson screening masses are fit to Eq. (3.4), which equates the screening masses for the two helicity components and fixes a common intercept. The nucleon screening masses are fit to straight lines with a common intercept.

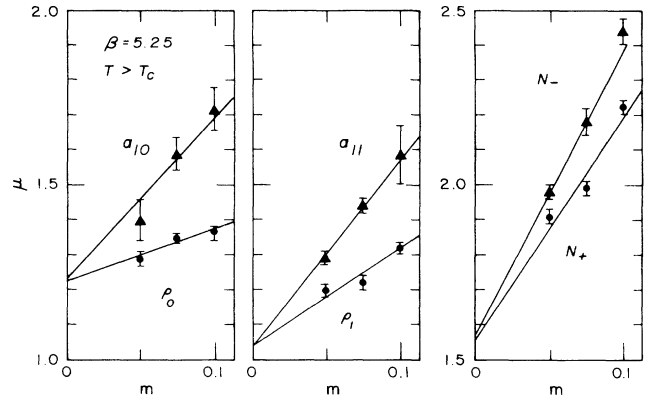


FIG. 8. As in Fig. 6, but at $\beta=5.25$. The ρ - and a_1 -meson screening masses are fit to straight lines with a common intercept, and the two helicity states are distinguished here. The nucleon screening masses are also fit to straight lines with a common intercept.

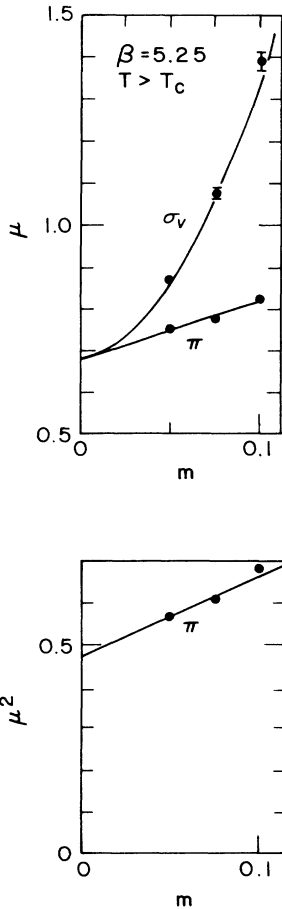


FIG. 7. As in Fig. 5, but at $\beta=5.25$. The pion screening mass is fit to a straight line and the σ screening mass, to Eq. (3.5) with the same intercept as the pion.

$$\mu_\pi(m) = 0.445(4) + 3.6(5)m \tag{3.3}$$

with $\chi^2/DF=2.9/1$, as plotted in Fig. 5. Also plotted are the squares of the pion screening masses. Clearly, an extrapolation of these points also results in a nonzero intercept. Therefore, it is apparent that the pionic mode is not a Goldstone boson at $\beta=5.175$. The σ meson screening mass extrapolates linearly at $\mu_\sigma(0)=0.50(4)$, a value within nearly 1 standard deviation of the pion intercept. Repeating the fits, this time enforcing a common intercept, yields the lines shown in Fig. 5 with $\chi^2/DF=1.8/3$, and a common intercept of $0.445(4)$.

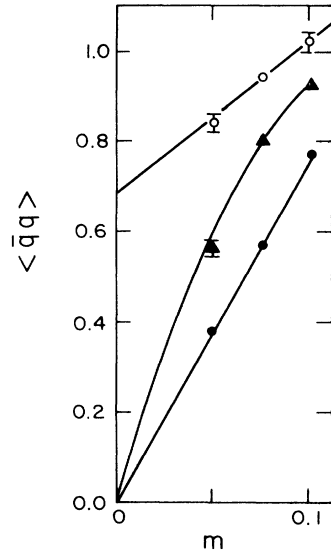


FIG. 9. Measurements of $\langle \bar{q}q \rangle$ as a function of bare-quark mass m for $\beta=5.10$, open circle, $\beta=5.175$, triangles, and $\beta=5.25$, solid circle. The fitted curves are described in Sec. III.

TABLE VII. A variety of expectation values: $plq = 1 - \text{Tr}UUUU/3$, Wilson line, chiral-order parameter, fermion energy density, and gauge-field energy density.

β	m	plq	W	$\langle \bar{q}q \rangle$	ϵ_F/T^4	ϵ_B/T^4
5.10	0.05	0.520(2)	0.009(3)	0.84(2)	-16(9)	-0.4(4)
	0.075	0.5243(7)	0.013(2)	0.94(1)	-4(5)	0.5(3)
	0.10	0.5332(5)	0.010(2)	1.00(2)	8(4)	-4(4)
5.175	0.05	0.483(1)	0.073(11)	0.56(2)	-1(4)	6(2)
	0.075	0.4982(4)	0.017(2)	0.80(1)	3(5)	5(2)
	0.10	0.5064(8)	0.012(3)	0.92(1)	-4(7)	-3(4)
5.25	0.05	0.4617(1)	0.238(3)	0.375(3)	8(3)	16(3)
	0.075	0.4687(4)	0.153(6)	0.568(9)	-3(4)	13(3)
	0.10	0.4820(3)	0.030(4)	0.764(9)	-1(4)	4(2)

Therefore, the results are consistent with a degeneracy of the π - σ chiral multiplet.

A linear extrapolation of the ρ and a_1 screening masses in each helicity channel yields values within 1 or 2 standard deviations of each other. As with the $\beta=5.10$ screening masses, the differences between the helicity channels is insignificant. Combining the results for the two helicity channels permits a linear extrapolation:

$$\begin{aligned} \mu_\rho(m) &= 1.11(9) + 3.5(11)m, \\ \mu_{a_1}(m) &= 1.17(6) + 6.7(10)m. \end{aligned} \quad (3.4)$$

Since the intercepts are statistically consistent with equality, we refit with a forced common intercept, obtaining a common screening mass of 1.15(5) with $\chi^2/\text{DF}=4.6/3$, as plotted in Fig. 6.

The nucleon screening masses are consistent with parity doubling in the chiral limit. Refitting these masses with a forced common intercept yields $\mu_N(0)=1.86(4)$ with $\chi^2/\text{DF}=1.5/3$, as plotted in Fig. 6.

Turning finally to an extrapolation of $\langle \bar{q}q \rangle$, we find from Table VII and Fig. 9 that this quantity shows strong curvature as a function of quark mass. Constraining its value to be zero and fitting the points to a quadratic yields

$$\langle \bar{q}q \rangle(m) = 14.4(4)m - 51(5)m^2$$

with $\chi^2/\text{DF}=7/1$, as shown in Fig. 9. The largest contribution to χ^2 comes from the lowest-mass point, which is least well-determined statistically, and lies in the crossover region. Using the slightly higher value for $\langle \bar{q}q \rangle$ found by Kogut and Sinclair⁶ at this point would improve the fit. Therefore, despite the large χ^2 in this instance we have confidence in our conclusion that an extrapolation to the chiral limit at this value of β leads to a phase in which chiral symmetry is manifest in the spectrum.

$\beta=5.25$. Finally, we turn to a chiral extrapolation of the screening masses at the highest temperature in this study. The pion screening mass again extrapolates to a value clearly distinct from zero. The σ -meson screening mass requires a quadratic extrapolation, as can be seen from Fig. 7. Constraining the intercept for the σ meson to equal the pion screening mass intercept yields the fit

$$\mu_\sigma(m) = 0.674 + 1.0(2)m + 59(3)m^2 \quad (3.5)$$

at $\chi^2/\text{DF}=3.3/1$, a fairly good fit.

The vector- and axial-vector-meson screening masses are statistically consistent with equality in the chiral limit. Forcing the two zero-helicity masses to have a common intercept yields $\mu_{\rho_0}(0)=\mu_{a_{10}}(0)=1.21(4)$ at $\chi^2/\text{DF}=2.2/3$, and the two helicity-one masses, yields $\mu_{\rho_1}(0)=\mu_{a_{11}}(0)=1.05(4)$ at $\chi^2/\text{DF}=3.9/3$. The constrained fits are shown in Fig. 8. Therefore, our results are statistically consistent with a ρ - a_1 degeneracy in the

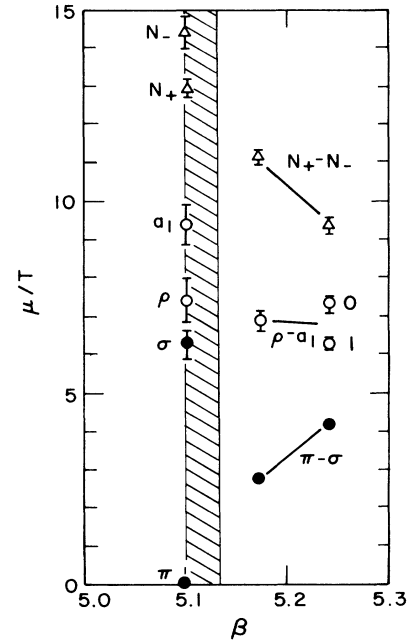


FIG. 10. Screening masses, expressed in units of the temperature, as extrapolated to the chiral limit, for the π -, σ -, ρ -, and a_1 -meson plasmon modes, and the lowest even-parity (N_+) and odd-parity (N_-) baryon plasmon modes, plotted as a function of the gauge-coupling β . Increasing β corresponds to increasing temperature. The shaded region indicates the possible location of the phase transition. The notation "0" and "1" beside the highest-temperature vector-axial-vector-meson mass indicates the helicity assignment.

TABLE VIII. Summary of screening masses in the chiral limit with constraints. Here masses are given in units of the temperature.

β	π	σ_v	ρ_0	ρ_1	a_{10}	a_{11}	$N(\frac{1}{2}^+)$	$N(\frac{1}{2}^-)$
5.10	0	6.2(4)	7.4(6)	7.4(6)	9.4(5)	9.4(5)	12.9(2)	14.4(4)
5.175	2.67(2)	2.67(2)	6.9(3)	6.9(3)	6.9(3)	6.9(3)	11.2(2)	11.2(2)
5.25	4.04(4)	4.04(4)	7.3(1)	6.3(2)	7.3(1)	6.3(2)	9.3(2)	9.3(2)

chiral limit. Our results also suggest a separation of the two helicity states.

Table VI shows that the two nucleon states of opposite parity are also likely to be in the same multiplet. Forcing them to have a common intercept gives a fitted value of $\mu_N(0) = 1.56(4)$ with $\chi^2/\text{DF} = 18/3$, as shown in Fig. 8. A quadratic fit could improve this χ^2 .

A linear fit to $\langle \bar{q}q \rangle$ without constraint gives an intercept of $0.002(10)$ at $\chi^2/\text{DF} = 0.5/1$, a result nicely consistent with zero. (See Fig. 9.) Therefore, the spectrum and $\langle \bar{q}q \rangle$ are all consistent with a restoration of $\text{SU}(N) \times \text{SU}(N)$ chiral symmetry.

C. Temperature dependence of the spectrum in the chiral limit

Collected in Fig. 10 and Table VIII are the results of the chiral extrapolation of the various screening masses. Here masses are expressed as a multiple of the temperature $T = \frac{1}{6}$ (lattice units). Evidence for asymptotic scaling for lattices of this size is scant.²² Therefore, the coupling-constant value is not converted to a temperature in this figure. However, increasing β corresponds to increasing temperature. If we were to use the asymptotic scaling expression

$$a \Lambda_L = (8\pi^2\beta/25)^{231/625} \exp(-4\pi^2\beta/25),$$

then the points $\beta = 5.10, 5.175, \text{ and } 5.25$ correspond to the temperatures $T/\Lambda_L = 188, 210, \text{ and } 235$, or $T/\Lambda_{\overline{\text{MS}}} = 2.47, 2.76, \text{ and } 3.09$, respectively ($\overline{\text{MS}}$ denotes the modified minimal subtraction scheme), for a temperature increase of 25% over the range of couplings considered. The σ -meson screening mass shows the most dramatic variation with temperature. Since correlations in the chiral-order parameter $\langle \bar{q}q \rangle$ are mediated by this meson, such behavior might be expected for a phase transition that restores the chiral symmetry. The pion screening mass is increasing more rapidly than linearly in temperature over this range of β , but it is not possible with these data to tell the size of the discontinuity in the pion screening mass at the phase transition. Finally, it is remarkable that all of the screening masses in the chirally symmetric phase over this range of gauge couplings are rather large—namely, a few to several times the temperature.

IV. CONCLUSIONS AND DISCUSSION

Our results are consistent with a restoration of an $\text{SU}(N) \times \text{SU}(N)$ chiral symmetry. In particular, we find good numerical evidence in the chiral limit of our model that (1) there is a cleanly identifiable pion plasma mode

in the high-temperature phase, (2) the expected π - σ and ρ - a_1 multiplets occur in the plasma, and, finally, (3) there are parity-doubled baryon plasma modes with a finite screening length for $T > T_c$.

The static pion correlation shows a remarkably clean fit to a single spectral component over six decades. If there were a $q\bar{q}$ component in this channel it would have a continuum threshold screening mass of at least twice the lowest fermion Matsubara frequency; namely, $2\pi T = 1.05$. Since the pionic spectral component seen in Fig. 2 is obviously of a considerably lower screening mass, it cannot be due to such a quark continuum. However, we cannot rule out the possibility that such a continuum occurs in addition to the pionic mode as a higher spectral component.

Our finding of parity doubling and a nonzero screening mass in the baryon channel in conjunction with a nonzero screening mass for the pion is in accordance with spectral inequality theorems.²³

A partial restoration of the U(1) axial symmetry, associated with the diminution of the gauge anomaly, would require a further parity doubling of the π - σ multiplet.¹⁶ However, we have not examined the relevant channels, and so cannot draw any conclusions regarding the fate of this symmetry.

Our results strongly suggest the existence of hadronic modes in the plasma screening spectrum. Further work is needed to provide a more detailed picture of the temperature dependence of the screening masses, to look for asymptotic scaling of the mass-temperature ratios, to study models with a more realistic quark spectrum, and to search for other hadronic modes, particularly the η - and η' -meson modes, to determine the fate of the U(1) axial symmetry.

The most urgent question, whether the modes that we observe are also important as real-time excitations of the plasma, will probably not be answered soon by lattice-gauge theory. The most promising lattice investigations that will help answer this question indirectly are studies of the QCD phase diagram. The spectral significance of a gap in the phase diagram was emphasized in the Introduction. For the moment we conclude that our findings of hadronic modes in the screening spectrum deals a serious blow to the naive deconfinement picture and requires a reconsideration of several of its predictions of the experimental plasma signature.

Note added in proof. In a closely related study substantially similar results were announced for two quark flavors, while this work was going to press. [See S. Gottlieb, W. Liu, D. Toussaint, R. L. Renken, and R. L. Sugar, University of California, San Diego Report No. UCSD-PTH-87/16 (unpublished).]

ACKNOWLEDGMENTS

This work was supported in part by the National Science Foundation under Grants Nos. NSF-PHY84-05648 and NSF-PHY82-01948 and by the San Diego Supercomputer Consortium. We would like to thank the San Diego Supercomputer Center and the Illinois National

Center for Supercomputer Applications for their assistance and access to the Crays at these centers. In particular, we thank Lex Layne at the NCSA for his help. C.D. thanks Al Mueller, Doug Toussaint, Yong Shi Wu, Tom DeGrand, and Paul MacKenzie for helpful comments and suggestions.

- ¹For a recent conference proceedings, see *Proceedings of the Fifth International Conference on Ultra-Relativistic Nucleus-Nucleus Collisions*, Pacific Grove, California, 1986, edited by L. S. Schroeder and M. Gyulassy [Nucl. Phys. **A461**, Nos. 1 and 2 (1987)]. For a review of QCD calculations, see H. Satz, Annu. Rev. Nucl. Part. Sci. **35**, 245 (1985).
- ²D. J. Gross, R. D. Pisarski, and L. G. Yaffe, Rev. Mod. Phys. **53**, 43 (1981); K. Kajantie and J. Kapusta, Ann. Phys. (N.Y.) **160**, 477 (1985); T. Appelquist and R. Pisarski, Phys. Rev. D **23**, 2305 (1981); S. Nadkarni, *ibid.* **27**, 917 (1983); J. Polónyi and H. Wyld, University of Illinois at Urbana-Champaign, Report No. ILL-TH-85-23 (unpublished); Massachusetts Institute of Technology Report No. CTP 1458, 1987 (unpublished); U. Heinz, K. Kajantie, and T. Toimela, Research Institute Theoretical Physics, University of Helsinki, Technical Report, 1986 (unpublished); T. H. Hansson and I. Zahed, Phys. Rev. Lett. **58**, 2397 (1987); S. Nadkarni, Rutgers University Report No. RU-87-22 (unpublished).
- ³C. E. DeTar, Phys. Rev. D **32**, 276 (1985).
- ⁴T. Hatsuda and T. Kunihiro, Phys. Rev. Lett. **55**, 158 (1985); Phys. Lett. B **185**, 304 (1987), and references therein.
- ⁵C. Chen, C. DeTar, and T. DeGrand, University of Utah Report No. UU-HEP-87/6 (unpublished).
- ⁶J. B. Kogut and D. K. Sinclair, Nucl. Phys. **B280**, 625 (1987).
- ⁷E. V. E. Kovacs, D. K. Sinclair, and J. B. Kogut, Phys. Rev. Lett. **58**, 751 (1987).
- ⁸M. Fukugita and A. Ukawa, Phys. Rev. Lett. **57**, 503 (1986); R. Gupta, G. Guralnik, G. W. Kilcup, A. Patel, and S. R. Sharpe, *ibid.* **57**, 2621 (1986); R. V. Gavai, Nucl. Phys. **B269**, 530 (1986); R. V. Gavai, J. Potvin, and S. Sanielevici, Phys. Rev. Lett. **58**, 2519 (1987); J. B. Kogut, H. W. Wyld, F. Karsch, and D. K. Sinclair, Phys. Lett. B **188**, 353 (1987); S. A. Gottlieb *et al.*, Phys. Rev. Lett. **59**, 1513 (1987).
- ⁹We thank Gordon Baym for a discussion of this point.
- ¹⁰J. Kogut and L. Susskind, Phys. Rev. D **11**, 395 (1975).
- ¹¹J. Polónyi and H. W. Wyld, Phys. Rev. Lett. **51**, 2257 (1983); S. Duane and J. B. Kogut, *ibid.* **55**, 2774 (1985); J. B. Kogut, Nucl. Phys. **B270** [FS16], 169 (1986).
- ¹²J. P. Gilchrist, H. Schneider, G. Schierholz, and M. Teper, Phys. Lett. **136B**, 87 (1984).
- ¹³H. Hamber and G. Parisi, Phys. Rev. D **27**, 208 (1983); M. Fukugita, S. Ohta, Y. Oyanagi, and A. Ukawa, National Laboratory for High Energy Physics (KEK) Report No. KEK-TH 150, 1987 (unpublished).
- ¹⁴A. Billoire, E. Marinari, A. Morel, and J. P. Rodrigues, Phys. Lett. **148B**, 166 (1984); A. Morel and J. P. Rodrigues, Nucl. Phys. **B247**, 44 (1984).
- ¹⁵E. T. Tomboulis and L. G. Yaffe, Phys. Rev. Lett. **52**, 1173 (1984).
- ¹⁶R. Pisarski and F. Wilczek, Phys. Rev. D **29**, 338 (1984).
- ¹⁷C. DeTar and J. Kogut, Phys. Rev. Lett. **59**, 399 (1987).
- ¹⁸The residual tolerance in the conjugate-gradient solution of the microcanonical evolution equation is defined as $\|a^\dagger a \psi - b\|^2$, where a is the usual staggered fermion Dirac operator, ψ is the time derivative of the pseudofermion field, and b is the inhomogeneous term in the microcanonical evolution. The squared norm is defined as the sum of the squares of all $3 \times 6 \times 10^3$ vector components. The residual tolerance in the determination of the quark propagator is defined as $\|a^\dagger a g - e\|^2$, where e is the unit vector and g is the desired propagator.
- ¹⁹H. Kluberg-Stern, A. Morel, O. Napoly, and B. Petersson, Nucl. Phys. **B220**, 447 (1983); J. Kogut, M. Stone, H. W. Wyld, S. H. Shenker, J. Shigemitsu, and D. K. Sinclair, *ibid.* **B225** [FS9], 326 (1983).
- ²⁰T. A. DeGrand and C. E. DeTar, Phys. Rev. D **34**, 2469 (1986).
- ²¹H. H. Harman, *Modern Factor Analysis* (University of Chicago Press, Chicago, 1960).
- ²²J. B. Kogut, Phys. Rev. Lett. **56**, 2557 (1986).
- ²³D. Weingarten, Phys. Rev. Lett. **51**, 1830 (1983); S. Nussinov, *ibid.* **51**, 2081 (1983); C. Vafa and E. Witten, *ibid.* **51**, 2351 (1983).